Journal of Power Sources 196 (2011) 5168–5173

Contents lists available at ScienceDirect

Journal of Power Sources

journal homepage: www.elsevier.com/locate/jpowsour

On the decrepitation mechanism of MgNi and $LaNi_5$-based electrodes studied by in situ acoustic emission

A. Etiemble[a,b], H. Idrissi[b,*], L. Roué[a,**]

[a] INRS-Énergie, Matériaux et Télécommunications, Varennes, Québec, J3X1S2 Canada
[b] MATEIS – Équipe CorrIS, INSA-Lyon, 69621 Villeurbanne Cedex, France

ARTICLE INFO

Article history:
Received 14 December 2010
Received in revised form 27 January 2011
Accepted 29 January 2011
Available online 22 February 2011

Keywords:
Acoustic emission
Particle cracking
Metal hydride electrodes
Ni-MH batteries

ABSTRACT

In situ monitoring of the pulverization of amorphous MgNi and crystalline $LaNi_5$-based alloys has been studied during their hydrogen charge by combining acoustic emission and electrochemical measurements. In both alloys, two classes of acoustic signals with specific temporal and energetic characteristics were detected during their charge: a P1 class related to the particle cracking and a P2 class due to the release of H_2 bubbles. By comparing the P1 activity on both materials as a function of the charge input, it was shown that the pulverization phenomenon becomes significant at a much lower charge input for the $LaNi_5$-based electrode (~5–25 mAh g^{-1}) than for the MgNi electrode (~365 mAh g^{-1}), reflecting the fact that the mechanism responsible of their decrepitation is not similar. Indeed, it was demonstrated that the cracking of the amorphous and porous MgNi material is mainly induced by the hydrogen evolution reaction whereas for the crystalline and denser $LaNi_5$-based material, the α–β lattice expansion is responsible of its decrepitation. It was also shown that the particle size and the charge current density have a major impact on the MgNi decrepitation. The correlation between the MgNi particle cracking and the discharge capacity decay with cycling was established.

1. Introduction

In Ni-MH batteries, the repeated volume expansion/contraction of the metal hydride (MH) upon cycling causes its fracture into smaller particles. In the case of $LaNi_5$-based hydrides, this decrepitation phenomenon leads to their activation by breaking the native surface oxide layer and by increasing the effective surface area of the electrode [1] but it also decreases their cycle life by increasing the alloy corrosion rate [2]. Presently, $LaNi_5$-based alloys used in commercial Ni-MH batteries are multicomponent alloys in which the various substituents for La and Ni help to increase the electrode cycle life by reducing the alloy expansion (and thus, its cracking) hence improving their corrosion resistance. In the case of MgNi-based electrodes, the decrepitation process intensifies the irreversible oxidation of the active material by the KOH electrolyte (*i.e.*, formation of $Mg(OH)_2$), which greatly decreases the electrode cycle life [3]. It was demonstrated that the major key to significantly improving the cycle life of MgNi-based electrodes is to limit their pulverization upon cycling, for instance by controlling the charge input [4] or by optimizing the initial particle size [5] and the alloy composition [6,7]. It has been assumed that the amorphous structure of the MgNi-based materials could increase their resistance to decrepitation by inducing a more gradual volume expansion upon hydrogen absorption than for crystalline compounds which are usually characterized by an abrupt α-to-β lattice expansion [4]. However, this assumption has never been experimentally confirmed.

The analysis of the decrepitation process is thus a key issue in the development of new metal hydrides for advanced Ni-MH batteries. In this context, we have recently demonstrated that acoustic emission (AE) techniques coupled to electrochemical measurements can be successfully applied for in situ monitoring of the cracking of MgNi and $LaNi_5$-based electrodes upon cycling [8]. In the present paper, the AE signals upon charging are analyzed in more detail by studying the evolution of the AE signals related to the MH pulverization and those due to the release of H_2 bubbles as a function of the charge input. On the basis of these new results, it will be shown for the first time that the mechanism responsible for pulverization is not the same for the amorphous MgNi and crystalline $LaNi_5$-based materials. Moreover, the influence of the particle size and charge rate on the cracking of the MgNi electrode will be presented.

* Corresponding author. Tel.: +33 4 72 43 89 20; fax: +33 4 72 73 87 15.
** Corresponding author at: INRS-Énergie, Matériaux et Télécommunications, 1650, bd. Lionel Boulet, Varennes, Québec, J3X1S2 Canada. Tel.: +1 450 929 8185; fax: +1 450 929 8102.
E-mail addresses: hassane.idrissi@insa-lyon.fr (H. Idrissi), roue@emt.inrs.ca (L. Roué).

0378-7753/$ – see front matter © 2011 Elsevier B.V. All rights reserved.
doi:10.1016/j.jpowsour.2011.01.098

2. Experimental

A commercial $LaNi_5$-based alloy ($MmNi_{3.68}Co_{0.78}Mn_{0.36}Al_{0.28}$) powder from Japan Metals & Chemicals Co. and an amorphous MgNi alloy powder obtained by high energy ball milling [4] were studied as active materials. 0.2 g of active material was manually mixed with 0.2 g of copper powder. The mixture was then cold pressed on 2 g of copper powder at 6 t cm^{-2} for 10 min in a stainless steel die to form a pellet (16 mm in diameter, ~2 mm in thickness) that will be used as working electrode.

The experimental set-up coupling AE and electrochemical measurements has been described elsewhere [8]. The reference electrode and the counter electrode were respectively an Hg/HgO electrode and a nickel wire. The three-electrode cell was monitored by a Voltalab PGZ 301 galvanostat/potentiostat. Unless otherwise indicated, the working electrode was charged at −100 mA g^{-1} for 3 h for the $LaNi_5$-based alloy and 5 h for MgNi, and discharged at 20 mA g^{-1} until reaching −0.6 V vs. Hg/HgO. All the experiments were carried out at room temperature in a 6 mol L^{-1} KOH solution. Before the first charge, the potential of the working electrode was maintained at −0.85 V vs. Hg/HgO for a few minutes to reduce the native oxide layer present on the Cu and active material powders.

The AE signals were recorded by a wide band sensor EPA micro 80 (frequency range 100–1000 kHz) and transmitted via an EPA USB Node acquisition card to the computer. For all the experiments, the gain *G* and the threshold *S* were fixed at 40 dB and 27 dB, respectively. The recorded acoustic signals were treated and the waveforms were obtained with AE Win software (EPA). From the acoustic waveform, characteristic parameters of the recorded signal were obtained, such as its amplitude *A*, its duration *D*, its rise time *R*, and its energy *E*. Rise time corresponds to the duration between the passing of the first threshold and the maximum signal amplitude. The energy is the integral of the squared amplitude over time of the signal duration and is expressed in term of energy units (eu). One eu means 10^{-14} V^2 s, corresponding to 10^{-18} J with a reference resistor of 10 kΩ. In addition, the fast Fourier transform (FFT) based spectral analysis of the AE signal enables the determination of the peak and barycentric frequencies.

The surface morphology of the electrodes before and after hydrogen charging was observed by scanning electron microscopy (SEM) using a Philips XL20 microscope.

3. Results and discussions

3.1. Characteristics of the P1 and P2 type acoustic signals

During the charge of the MH electrode, two classes of acoustic signals can be detected: the first one (labelled P1) is attributed to the cracking of the MH particles, and the second one (labelled P2) is due to the release of H_2 bubbles associated with the hydrogen evolution reaction (HER), as shown in our previous study [8]. No acoustic activity is detected during the discharge step. Fig. 1A shows the typical waveforms and associated power spectra of recorded P1 and P2 type signals on a MgNi electrode (first charge). The repartition of these two AE classes as a function of their rise time and energy is shown in Fig. 1B. Their respective characteristics are reported in Table 1. They slightly differ from those established in our previous work [8] due to the use of a different AE sensor (*i.e.*, EPA Micro 80 (100–1000 kHz) in the present study vs. Vallen AE 144A (100–500 kHz) in our previous work).

P1-type signals related to the MH pulverization exhibit short rise time and duration (<30 μs and <100 μs, respectively), high amplitude and energy (up to 70 dB and 100 eu, respectively) and a high peak frequency (250–350 kHz). P2-type signals resulting from the release of H_2 bubbles are characterized by a longer rise time and duration (up to 200 μs and 250 μs, respectively), lower amplitude and energy (<40 dB and <20 eu, respectively) and a lower peak frequency (80–150 kHz). Similar results were obtained on the $LaNi_5$-based electrode (not shown). In contrast, on a Cu electrode, only P2 acoustic signals related to the HER were detected [8]. These observations are in accordance with the study of Inoue et al. on $LaNi_5$-based and Cu electrodes showing that AE signals related to pulverization phenomena have shorter durations, larger amplitudes and higher peak frequencies than those generated from the HER [9]. They also agree with AE studies about hydrogen embrittlement on aluminium and steel [10,11].

Table 1
Main characteristics of recorded P1 and P2 type AE signals.

	P1	P2
Energy (eu)	Up to 100	<20
Amplitude (dB)	Up to 70	<40
Rise time (μs)	<30	Up to 200
Duration (μs)	<100	Up to 250
Frequency peak (kHz)	250–350	80–150

3.2. Evolution of the P1 and P2 activities during the first charge

The evolution of the electrode potential and the acoustic activity (number of events) of the P1 and P2 type AE signals as a function of the charge input during the first charge are shown in Fig. 2A and B for $LaNi_5$-based and MgNi electrodes, respectively. On the $LaNi_5$-based electrode (Fig. 2A), a rapid decrease of the electrode potential (from *ca.* −1.0 to −1.17 V vs. Hg/HgO) is observed up to a charge input of ~5 mAh g^{-1}. Then, the electrode potential slowly decreases, reaching a stable value around −1.23 V vs. Hg/HgO at a charge input of ~250 mAh g^{-1}. This slow potential evolution is associated with the hydrogen absorption reaction (HAR), leading to the formation of the β hydride $LaNi_5$-based phase. From a charge input of ~250 mAh g^{-1}, the $LaNi_5$-based electrode is fully charged and then, the HER becomes dominant. This is confirmed by the steep rise in the P2 acoustic activity related to the release of H_2 bubbles from 250 mAh g^{-1}. Concerning the P1 activity, an abrupt increase is observed from ~5 to 25 mAh g^{-1}, reaching a maximum cumulated number of ~3000 events at a charge input ~60 mAh g^{-1}. Almost no additional P1 events are observed during the rest of the charge period, except at the end of the charge (*i.e.*, from ~260 mAh g^{-1}) where a small increase in P1 activity is again observed. Thus, on the basis of the evolution of the P1 activity observed in Fig. 2A, it appears that the cracking of the $LaNi_5$-based particles mainly occurs between 5 and 25 mAh g^{-1}. Assuming that the totality of the charge input is consumed for the HAR, this represents an amount of hydrogen absorbed into the alloy of ~0.02–0.09 wt.%. On the basis of typical hydrogen pressure-composition isotherms for $LaNi_5$-based alloys [12], this corresponds to the hydrogen concentration range where the conversion of the α solid solution to the β hydride phase is initiated. In other words, this tends to indicate that the mechanical stress inducing the cracking of the $LaNi_5$-based alloy is concentrated at the α-to-β phase transition region. This is in accordance with the study of Notten et al. demonstrating from in situ XRD investigations on $LaNi_5$-based alloys that the discrete α–β lattice expansion rather than the total lattice expansion is responsible for the particle cracking [12].

On the MgNi electrode (Fig. 2B), one can observe a slow decrease of the potential (from *ca.* −0.90 to −1.00 V vs. Hg/HgO) due the HAR with a well-discernible plateau centred at *ca.* −0.95 V related to the α + β mixed region. The fact that the HAR occurs at more positive potentials than on the $LaNi_5$-based electrode (Fig. 2A) mainly results from the higher thermodynamic stability of the β hydride MgNi phase. When the electrode reaches its fully hydrogen charged

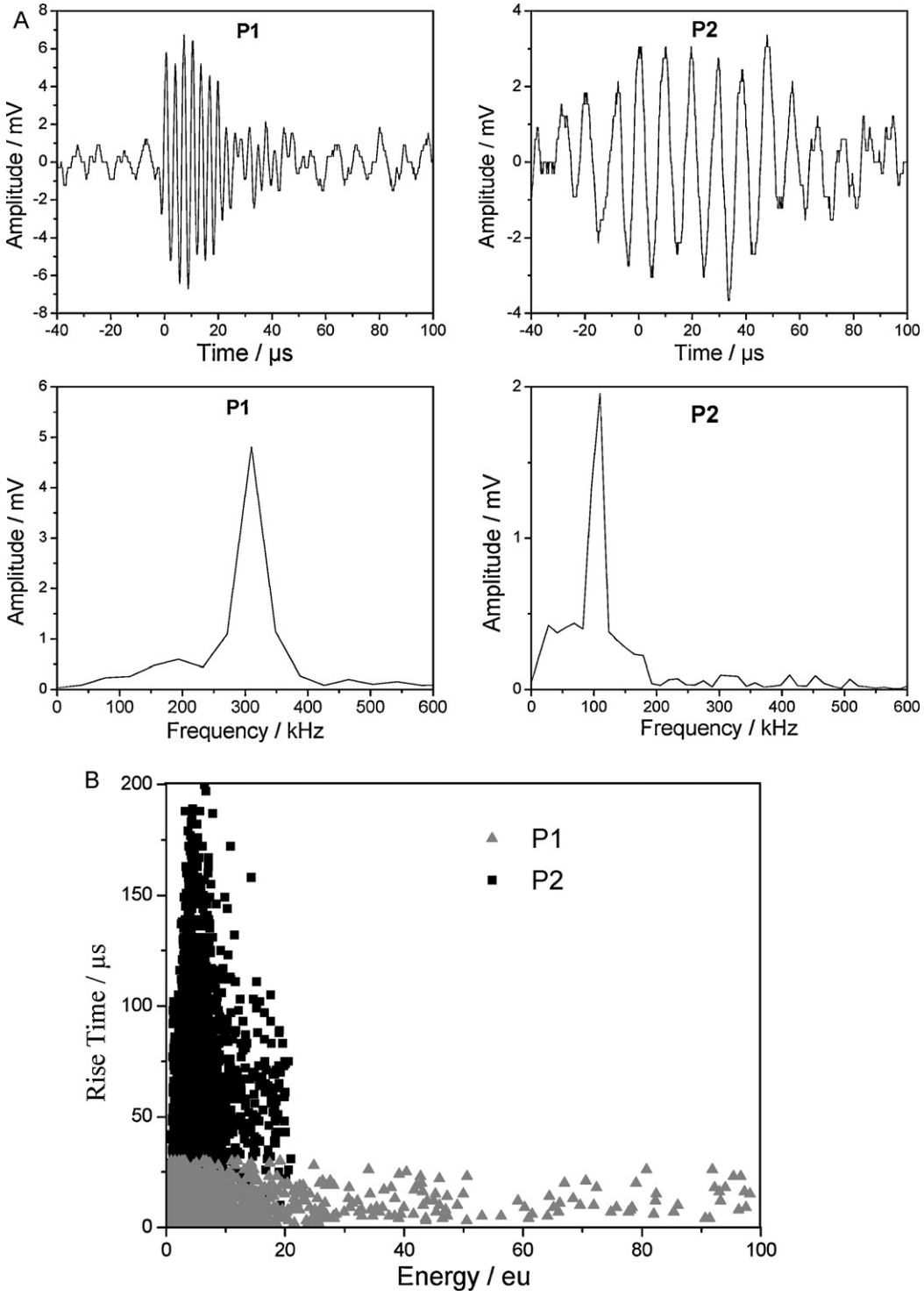

Fig. 1. (A) Typical waveforms and associated power spectra of recorded P1 and P2 type AE signals for a MgNi electrode (first charge); (B) repartition of the P1 and P2 classes as a function of their rise time and energy.

state (*i.e.*, at a charge input ~375 mAh g^{-1}), a stabilization of the potential (at *ca.* −1.0 V vs. Hg/HgO) due to the HER is observed. The evolution of the P1 activity with the charge input in Fig. 2B differs notably from that observed for the $LaNi_5$-based electrode (Fig. 2A). Indeed, a small increase of the P1 activity (up to a maximum of ~300 events) is observed from ~25 to 100 mAh g^{-1}. Then, no P1 activity is detected before reaching a charge input of ~365 mAh g^{-1} where an abrupt and large rise of the P1 activity (up to ~3000 events) is observed. At the same time, an important increase of the P2 acoustic activity related to the release of H_2 bubbles is detected. These observations suggest that the MgNi particle cracking is mainly induced by the hydrogen evolution reaction rather than by the α–β lattice expansion in contrast to what was previously observed for the $LaNi_5$-based material. It may be related to the particular morphology and structure of the MgNi powder. Indeed, the MgNi alloy produced by ball milling has an amorphous structure, which results in the absence of an abrupt α-to-β phase transition in this material during the HAR [13]. Consequently,

the mechanical stress related to volume expansion upon hydrogen absorption in amorphous MgNi is expected to be lower and more progressive than for the crystalline $LaNi_5$-based alloy. As a result, P1 activity in the α-to-β phase transition region (*i.e.*, between ~25 and 100 mAh g^{-1} corresponding to a H-content range of 0.09–0.37 wt.%) is much lower and more progressive (Fig. 2B) than for the $LaNi_5$-based alloy (Fig. 2A). On the other hand, ball-milled MgNi powder is constituted of porous agglomerates made up of many particles cold-welded together [5]. These agglomerates are likely to be broken down by the mechanical stress induced by the accumulation of H_2 bubbles into the pores during the HER. This is confirmed by the concomitant detection of the P1 and P2 type signals as shown in Fig. 2B.

3.3. Evolution of the electrode morphology with charging

SEM images of the surface of the $LaNi_5$-based and MgNi electrodes obtained after different charge inputs during the first cycle are shown in Fig. 3. The formation of many cracks is clearly observable on the $LaNi_5$-based alloy surface after a charge input of 50 mAh g^{-1} (Fig. 3B). No significant increase of the particle fracturing is observed when the charge input is extended to 300 mAh g^{-1} (Fig. 3C). On the other hand, the cracking of the MgNi particles appears very limited after a charge input of 150 mAh g^{-1} (Fig. 3E) whereas large cracks are observed after a charge input of 500 mAh g^{-1} (Fig. 3F). These results clearly confirm the correlation between the MH particle cracking and the large rise of the P1 activity displayed in Fig. 2.

3.4. Evolution of the P1 activity with cycling

Fig. 4A and B shows the evolution with cycling (5 cycles) of the P1 activity and the critical charge input (*i.e.*, the charge input inducing a large increase of the P1 activity) for $LaNi_5$-based (A) and MgNi (B) electrodes. On both electrodes, the P1 activity is maximum (~3300 events) during the first charge and falls to ~700 and ~300 events at the second cycle on $LaNi_5$-based and MgNi electrodes, respectively. No major variation of the P1 activity is observed during the subsequent cycles. This clearly indicates that the pulverization of the $LaNi_5$-based and MgNi electrodes mainly occurs during the first charge. Note that in a previous work [8], we have observed a maximum P1 activity at the second cycle on $LaNi_5$-based electrode. This discordance can be explained by the fact that in the present study, the electrode was polarized at −0.85 V vs. Hg/HgO before the first charge (see Section 2) in order to reduce the native oxide layer

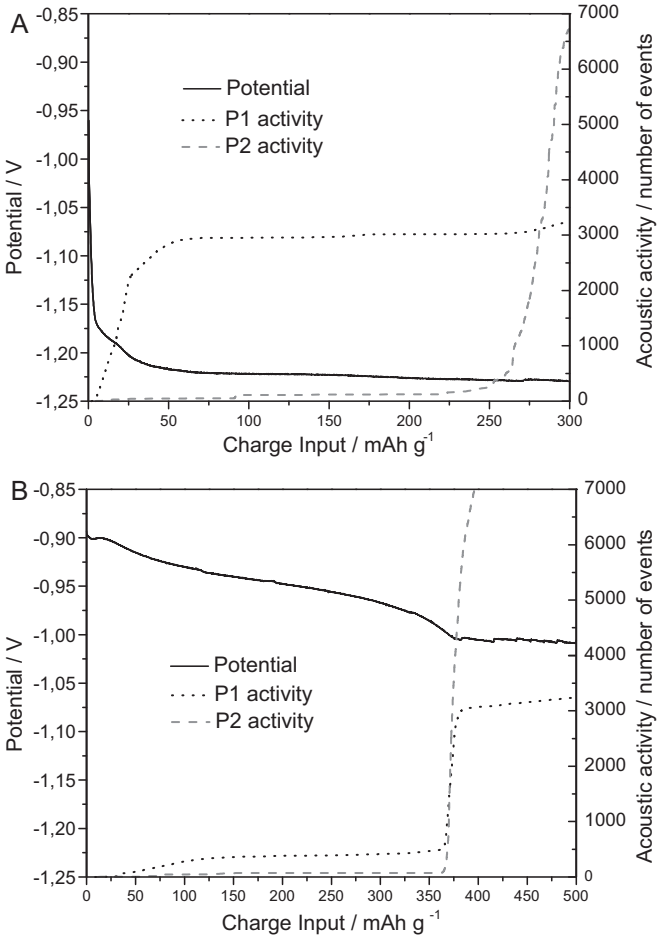

Fig. 2. Evolution of the electrode potential and the acoustic activity (number of events) of the P1 and P2 type AE signals as a function of the charge input during the first charge for (A) $LaNi_5$-based and (B) MgNi electrodes.

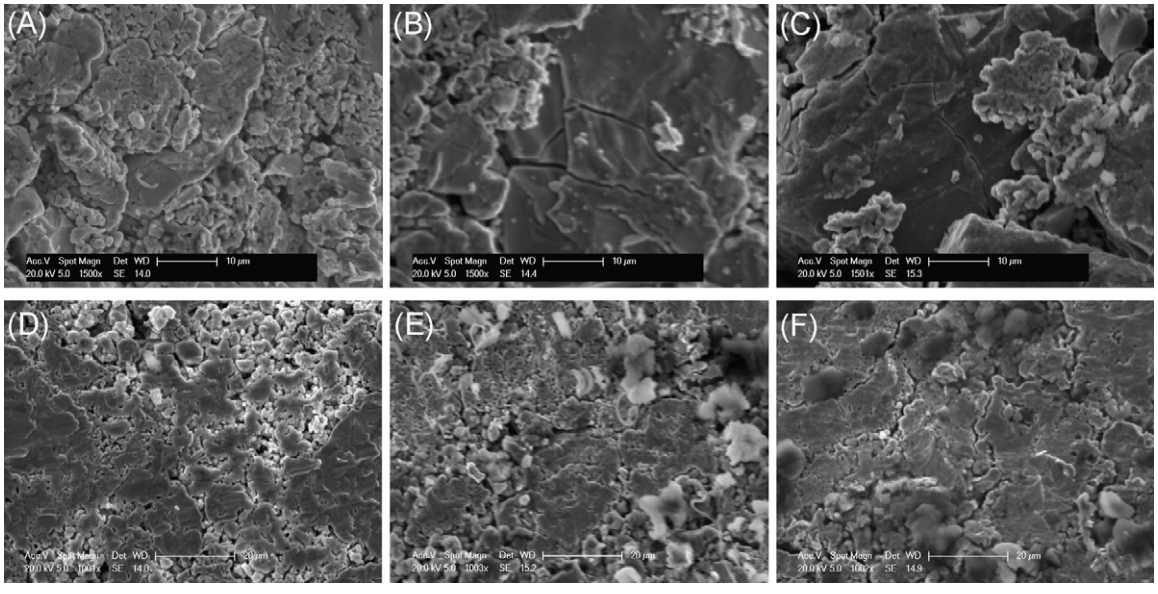

Fig. 3. SEM micrographs of a $LaNi_5$-based electrode before charging (A), after a charge input of 50 mAh g^{-1} (B) and 300 mAh g^{-1} (C) and of a MgNi electrode before charging (D), after a charge input of 150 mAh g^{-1} (E) and 500 mAh g^{-1} (F).

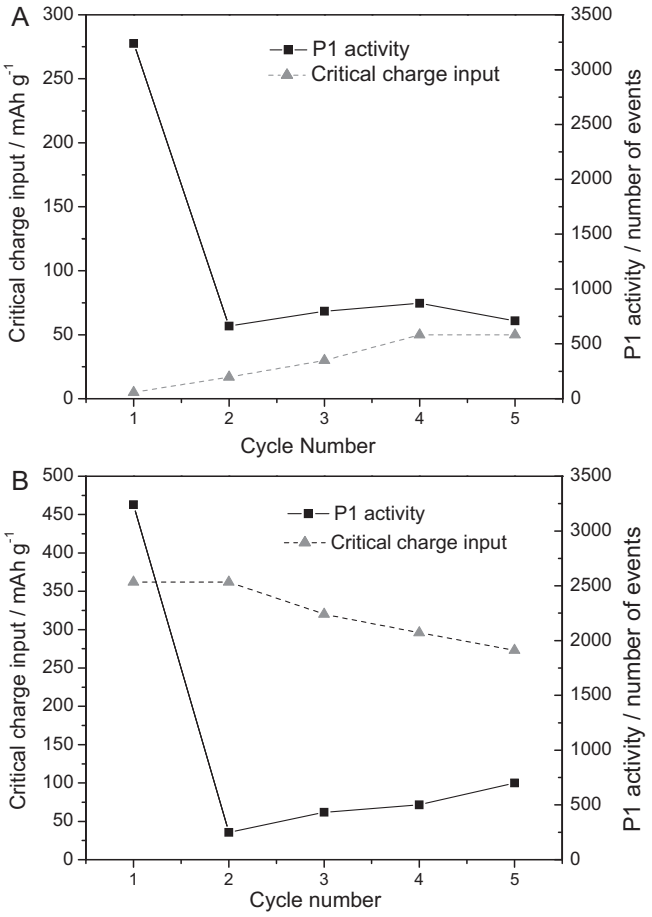

Fig. 4. Evolution with cycling of the P1 activity and the critical charge input for (A) $LaNi_5$-based and (B) MgNi electrodes.

present at the surface of the powder and thus, the electrode is active for the HAR from the first charge.

As seen in Fig. 4A, the critical charge input on the $LaNi_5$-based electrode increases from 5 mAh g^{-1} at the 1st cycle to 50 mAh g^{-1} at the 5th cycle. This may reflect an increase of the resistance to rupture of the active material with cycling because the strain related to its volume expansion would be easier to release as the particle size decreases with cycling. In contrast, as seen in Fig. 4B, the critical charge input decreases with cycling on the MgNi electrode (from 365 mAh g^{-1} at the 1st charge to 275 mAh g^{-1} at the 5th charge). This is related to the fact that the HER (inducing significant MgNi particle cracking as demonstrated previously) starts at lower charge input as the cycle number increases due the electrode degradation. This is confirmed by the evolution of the charge curves and P2 activity with cycling (not shown).

3.5. Influence of the charge rate on the MgNi cracking

As seen in Fig. 5A, the charge current density (*i.e.*, charge rate) has a profound effect on the P1 activity of the MgNi electrode measured during the first charge. Indeed, the cumulative P1 activity rises significantly with the increasing charge rate (from 3300 events at 100 mA g^{-1} to 14,000 events at 400 mA g^{-1}) whereas the critical charge input decreases from 365 mAh g^{-1} at 100 mA g^{-1} to 260 mAh g^{-1} at 400 mA g^{-1}. This can be related to the fact that the HER becomes more intense and appears earlier when the charge current density increases as seen in Fig. 5B, which compares the evolution of the P2 activity with the charge input for a charge current density of 100 and 400 mA g^{-1}. These results demonstrate that

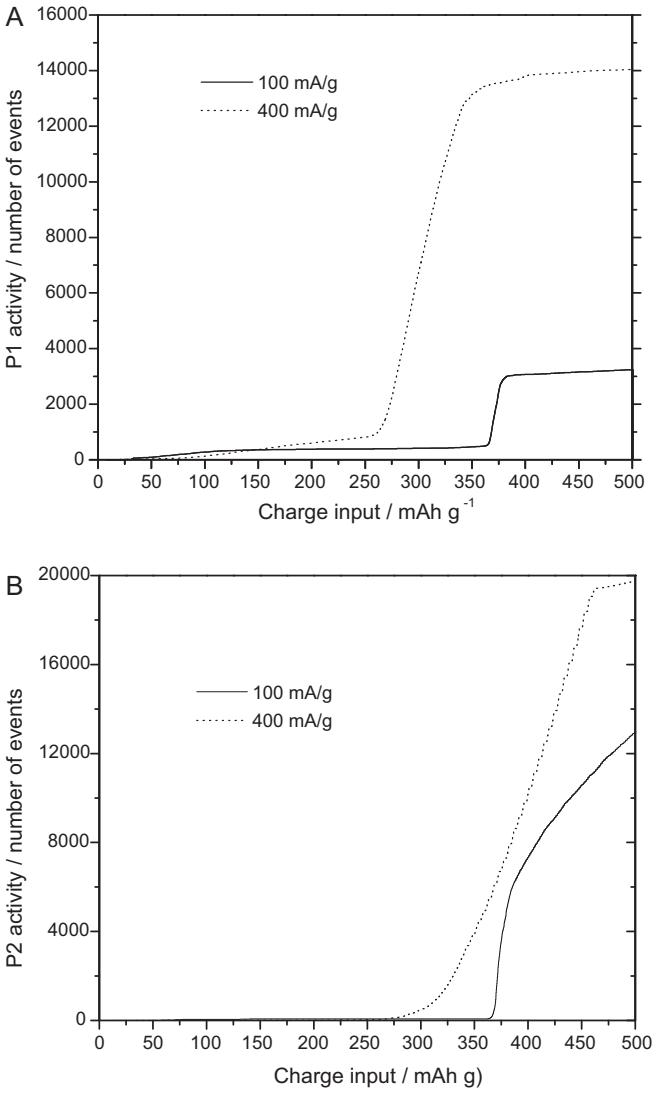

Fig. 5. Evolution of the (A) P1 and (B) P2 activities as a function of the charge input during the first charge for the MgNi electrode at a charge current density of 100 and 400 mA g^{-1}.

not only the depth of charge but also the charge rate has a major effect on the extent of the MgNi particle cracking.

3.6. Influence of the particle size on the MgNi cracking

The influence of the size of the MgNi particles on their cracking during the first charge is highlighted in Fig. 6 by comparing the evolution of the P1 activity with the charge input for electrodes made from <20 μm and >150 μm MgNi particle size fractions. It clearly appears that the P1 activity is more intense with the >150 μm particles than with the <20 μm ones. This may be due to the larger proportion of pores and lower mechanical strength for the bigger particles, resulting in a higher sensitivity to cracking by the H_2 bubbles. It can also be noted that no significant P1 activity is detected in the α-to-β phase transition region for the <20 μm particles, which agrees with the assumption that the volume expansion is easier to release as the particle size decreases. On the other hand, the critical charge input inducing cracking by H_2 evolution slightly increases with the particle size (380 mAh g^{-1} for >150 μm particles compared to 350 mA g^{-1} for <20 μm particles), which indicates that the HER appears later, as argued previously. This can be explained by the larger initial hydrogen storage capacity of the bigger MgNi parti-

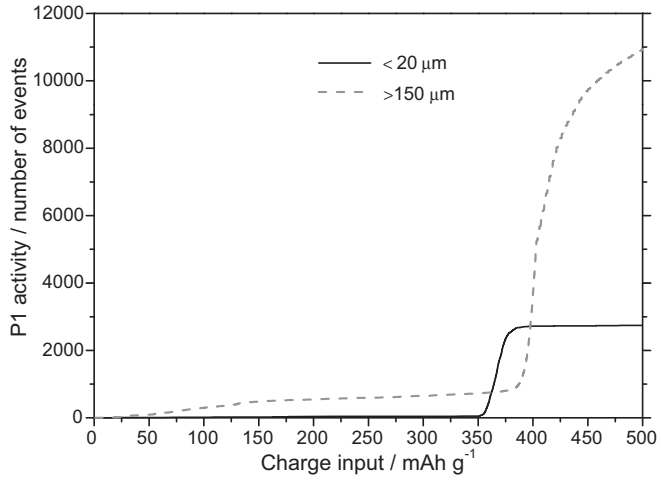

Fig. 6. Evolution of the P1 activity as a function of the charge input during the first charge for MgNi electrodes made from <20 μm and >150 μm particle size fractions.

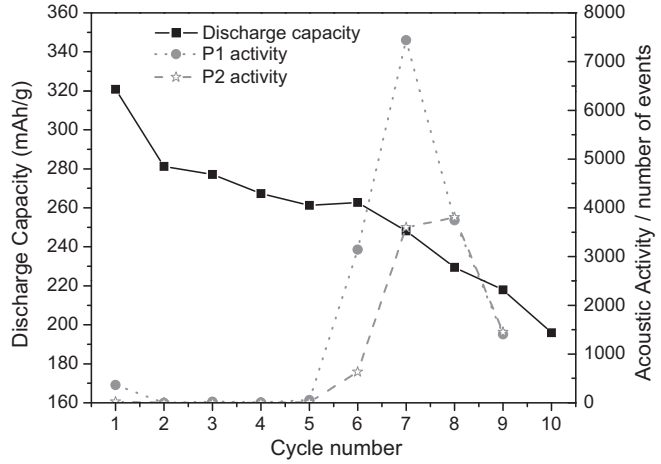

Fig. 7. Evolution with cycling of the P1 and P2 activities and the discharge capacity for a MgNi electrode charged at 300 mAh g^{-1}.

cles related to a less serious initial oxidation by the KOH electrolyte (*i.e.*, $Mg(OH)_2$ formation) due to their lower specific surface area [5].

3.7. Correlation between the particle cracking and the capacity decay of MgNi with cycling

Fig. 7 shows the evolution with cycling of the P1 and P2 activities and the discharge capacity for a MgNi electrode charged with a charge input of 300 mAh g^{-1} (at −100 mA g^{-1} for 3 h). The first cycle discharge capacity (320 mAh g^{-1}) is superior to the charge input (300 mAh g^{-1}). This surplus discharge capacity of 20 mAh g^{-1} can be explained by the anodic formation of $Mg(OH)_2$ and $Ni(OH)_2$ during the first discharge step [4]. From the 2nd to the 6th cycle, the discharge capacity slowly decreases with a mean capacity decay of 4 mAh g^{-1} per cycle. A significant increase of the capacity degradation rate is observed during the subsequent cycles with a mean capacity decay of 17 mAh g^{-1} per cycle from the 6th to the 10th. Regarding the acoustic signals, a small P1 activity is observed during the first cycle (detected in the α-to-β phase transition region) whereas no activity is observed between the 2nd and the 5th cycle. An important increase of the P1 activity (detected in the HER region) is observed from the 6th cycle, reaching a maximum at the 7th cycle and then decreasing progressively. The P2 activity related to the HER follows almost the same evolution with cycling, confirming that the MgNi particle cracking is mainly induced by the HER. It also confirms that the particle cracking process greatly accelerates the degradation of the electrode since the increase of the P1 activity and that of the discharge capacity decay are clearly linked in Fig. 7.

4. Conclusion

The study confirmed that acoustic emission techniques coupled to electrochemical measurements is an effective in situ method for studying the decrepitation of metal hydride electrodes for Ni-MH batteries. It was demonstrated that the process inducing the decrepitation of amorphous MgNi produced by ball milling differs notably from that of crystalline $LaNi_5$-based material. The decrepitation of this latter occurred at the beginning of the charge step (*i.e.*, in the α-to-β phase transition zone) whereas for MgNi, it mainly took place at the end of the charge step (*i.e.*, when the HER is initiated). It was also shown that the cracking of MgNi is accentuated as the particle size and the discharge current increase. On the basis on this study, it can be concluded that the future strategies to improve the decrepitation resistance of the ball-milled MgNi-based materials will have to be firstly focused on a reduction of their porosity in order to prevent their fracturing by the accumulation of H_2 bubbles in the particle pores during the HER.

Acknowledgment

This work was financially supported by the Natural Sciences and Engineering Research Council (NSERC) of Canada.

References

[1] P.H.L. Notten, R.E.F. Einerhand, J.L.C. Daams, J. Alloys Compd. 210 (1994) 221.
[2] J.J.G. Willems, Philips J. Res. 39 (1984) 1.
[3] S. Ruggeri, L. Roué, J. Huot, R. Schulz, L. Aymard, J.M. Tarascon, J. Power Sources 112 (2002) 547.
[4] S. Ruggeri, L. Roué, J. Power Sources 117 (2003) 260.
[5] C. Rongeat, L. Roué, J. Power Sources 132 (2004) 302.
[6] C. Rongeat, L. Roué, J. Electrochem. Soc. 152 (2005) A1354.
[7] C. Rongeat, S. Ruggeri, M.-H. Grosjean, M. Dehmas, S. Bourlot, L. Roué, J. Power Sources 158 (2006) 747.
[8] S. Didier-Laurent, H. Idrissi, L. Roué, J. Power Sources 179 (2008) 412.
[9] H. Inoue, R. Tsuzuki, S. Nohara, C. Iwakura, Electrochem. Solid-State Lett. 9 (2006) 504.
[10] F. Bellenger, H. Mazille, H. Idrissi, NDT Int. 35 (2002) 385.
[11] M. Perrin, L. Gaillet, C. Tessier, H. Idrissi, Corros. Sci. 52 (2010) 1915.
[12] P.H.L. Notten, J.L.C. Daams, R.E.F. Einerhand, J. Alloys Compd. 210 (1994) 233.
[13] S. Ruggeri, L. Roué, G. Liang, J. Huot, R. Schulz, J. Alloys Compd. 343 (2002) 170.